

Band Engineering via Gradient Molecular Dopants for CsFA Perovskite Solar Cells

Ziru Huang, Mingyang Wei, Andrew Harald Proppe, Hao Chen, Bin Chen, Yi Hou, Zhijun Ning, and Edward Sargent*

Perovskites with the multi-cation composition of cesium (Cs), methylammonium (MA), and formamidinium (FA) (CsMAFA) are pursued for their high power conversion efficiencies, but they are limited by their thermal stability. To withstand damp-heat accelerated aging MA-free compositions such as CsFA are of interest, but these exhibit lower carrier diffusion lengths and thus lesser performance in photovoltaic devices. A band engineering strategy that overcomes limited carrier diffusion within inverted perovskite solar cells based on CsFA is reported. A joint experimental-computational study shows that treating the perovskite with an n-type molecular dopant increases band bending, shaping the electric field across the active layer to overcome limited diffusive transport. Using this strategy, CsFA solar cell devices with stabilized power conversion efficiencies of 20.3%, a high value for devices using CsFA active layers, are fabricated.

1. Introduction

Metal halide perovskite solar cells (PSCs) have attracted great interest in recent years, with certified power conversion efficiencies now exceeding 25%, approaching the best single-junction silicon solar cells.^[1] The highest-performance PSCs use active layers with mixed cation and anion compositions, combining methylammonium (MA), formamidinium (FA), cesium (Cs) as cations and bromine and iodine as anions.^[2–4]

Despite progress in device efficiency, high performance PSCs require further progress in stability and aging tests, such as the International Electrotechnical Commission (IEC) 61646 standard.^[5] The damp heat test (85 °C and 85% humidity for 1000 h) is particularly challenging.^[6,7] The highest performing PSCs use MA, a volatile species that degrades to CH₃I and NH₃ at temperatures as low as 80 °C.^[8] To date, these PSCs

that have passed the damp heat test have relied on MA-free compositions that improve thermal stability, but these have so far done so at a cost to efficiency.^[6,9–11] In the case of CsFA, lower performance is assigned to a limited diffusion length compared to CsFAMA.^[12]

Herein we report a band engineering strategy to address the limited carrier diffusion in CsFA perovskites. Optoelectronic simulations reveal how gradient n-type doping in the perovskite layer reshapes the electric field profile, an approach we then implement in devices. Using the molecular dopant 4-(1,3-dimethyl-2,3-dihydro-1H-benzimidazol-2-yl)-N,N-diphenylaniline (N-DPBI) in the perovskite layer to tune the band bending and alignment, we obtain

increased charge carrier extraction leading to PSCs with a stabilized output (SPO) of 20.3% using a thermally stable active layer, a high efficiency for CsFA-based devices.

2. Results and Discussion

We first investigated the thermal stability of CsFA (formula of Cs_{0.1}FA_{0.9}PbI_{2.7}Br_{0.3}) perovskite thin films. X-ray diffraction (XRD) patterns of fresh and aged (70 h at 85 °C) perovskite films are shown in **Figure 1**. CsFA films showed no noticeable change following thermal annealing, whereas for the CsMAFA film (formula Cs_{0.05}MA_{0.14}FA_{0.819}PbI_{2.55}Br_{0.45}), there is an appreciable increase in the intensity of the PbI₂ peak: The ratio of peak areas for PbI₂ and perovskite increased from 0.35 to 0.42 (a detailed comparison of the PbI₂ and perovskite peak areas is given in Table S1, Supporting Information). In sum, the CsMAFA composition is prone to heat induced degradation, whereas the CsFA perovskite remains stable at temperatures of 85 °C.

CsFA PSCs exhibit performance inferior to that of solar cells based on CsMAFA, and prior studies have shown that this occurs due to poorer carrier diffusion within the active layer.^[12] To check whether carrier extraction does truly limit performance in devices, we collected photoluminescence (PL) lifetimes (**Figure 2**) in order to estimate the carrier diffusion length, L_D , according to the following formula:^[13]


$$L_D = \frac{2L}{\pi} \sqrt{2 \left(\frac{\tau}{\tau_q} - 1 \right)} \quad (1)$$

Z. Huang, Dr. M. Wei, Dr. A. H. Proppe, Dr. B. Chen, Dr. Y. Hou, Prof. E. Sargent

Department of Electrical and Computer Engineering
University of Toronto

35 St. George Street, Toronto, Ontario M5S 1A4, Canada
E-mail: ted.sargent@utoronto.ca

Dr. H. Chen, Prof. Z. Ning
School of Physical Science and Technology
ShanghaiTech University
Shanghai 201210, P. R. China

 The ORCID identification number(s) for the author(s) of this article can be found under <https://doi.org/10.1002/adfm.202010572>.

DOI: 10.1002/adfm.202010572

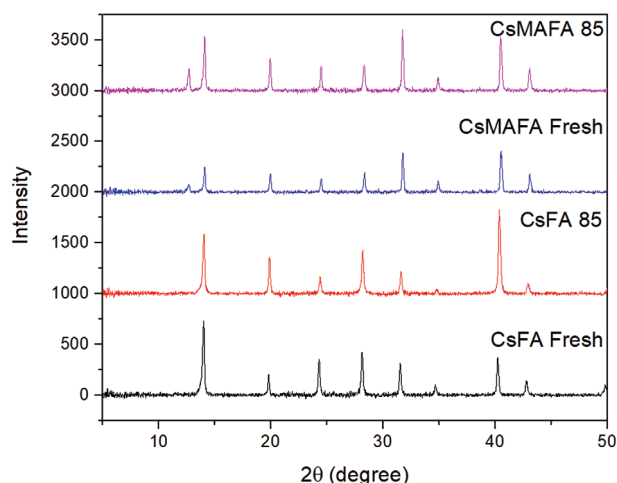


Figure 1. XRD patterns of CsFA and CsMAFA perovskite films before and after annealing at 85 °C for 70 h.

where L is the film thickness, τ is the unquenched PL lifetime, and τ_q is the quenched PL lifetime. In our experiments, we used spin-coated PCBM as an electron-selective quenching layer on top of the perovskite film. The perovskite films used in PL measurements had thickness 300 ± 30 nm.

For CsMAFA, fitting yields $\tau_q = 92 \pm 1$ ns and $\tau = 8.0 \pm 0.5 \times 10^2$ ns, resulting in an estimated L_D of 7.5×10^2 nm, which is greater than the thickness of the perovskite active layers used in solar cells. For CsFA, we obtained $\tau_q = 106 \pm 1$ ns, $\tau = 462 \pm 4$ ns, yielding an L_D of $4.9 \pm 0.5 \times 10^2$ nm, shorter than CsMAFA and also insufficient to achieve high performance solar cells. The lower value of L_D in CsFA thin films is unfavorable in solar cells since carrier transport is dependent on diffusion, rather than drift, when the solar cell is working near the open circuit condition. When operating at the maximum power point (MPP), the energy bands of the solar cell are only slightly bent and carrier diffusion is still important. Another disadvantage we observe for CsFA is the longer τ_q , which suggests that

the charge transfer between the CsFA perovskite active layer and the electron transporting layer (ETL) is slower than that between CsMAFA perovskite and the ETL. Since charge trapping and nonradiative recombination are processes that compete with charge extraction, the slower charge transfer from the CsFA perovskite to the ETL allows more nonradiative recombination, which further deteriorates performance.

We posited that carrier transport within the CsFA perovskite active layer could be improved by manipulating the band bending in order to achieve an additional internal electrical field, under which carrier drift and transport to electrodes would be enhanced. We simulated a band-engineered condition of gradient n-type doping of the perovskite (described in detail in the Supporting Information), where the region of the perovskite conduction band minimum (CBM) close to the ETL was bent downwards such that the internal electrical field could help electrons in the perovskite migrate to the ETL. **Figure 3** shows the simulation results of conventional CsFA and band engineered CsFA PSCs. For band engineered CsFA (**Figure 3b**), the CBM of perovskite is bent more toward the lowest unoccupied molecular orbital of PCBM than for conventional CsFA (**Figure 3a**). Near MPP, increased band bending in the band-engineered device facilitates charge migration and reduces nonradiative recombination due to carriers that would otherwise fail to reach PCBM, thus improving the fill factor (FF). Our simulations show that Shockley–Read–Hall (SRH) recombination, one of the most prominent sources of nonradiative recombination in solar cells, is reduced by 50% in band-engineered devices compared to the unmodified device throughout most of the active layer region. This drastically reduced SRH recombination rate supported the potential of this band engineering method to improve the efficiency of PSCs based on active layers with poor carrier transport.

Encouraged by our simulations, we then sought to experimentally realize the proposed method. To tune the band bending within the perovskite, we added *N*-DPBI to the anti-solvent in order for it to penetrate into the perovskite during film crystallization. *N*-DPBI is an n-type molecular dopant, and

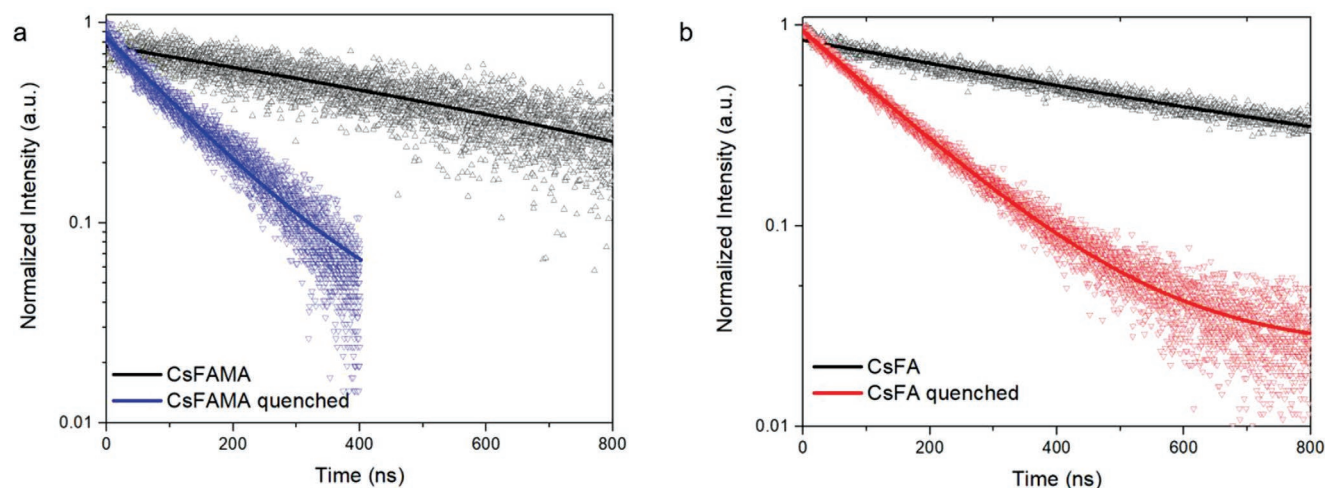


Figure 2. Comparison of quenched and unquenched PL lifetimes for the CsMAFA and CsFA perovskite films. a) PL lifetime of the CsMAFA and b) CsFA films. PCBM was used as an electron selective quenching layer atop the perovskite active layer. Films were photoexcited from the glass side of the substrate.

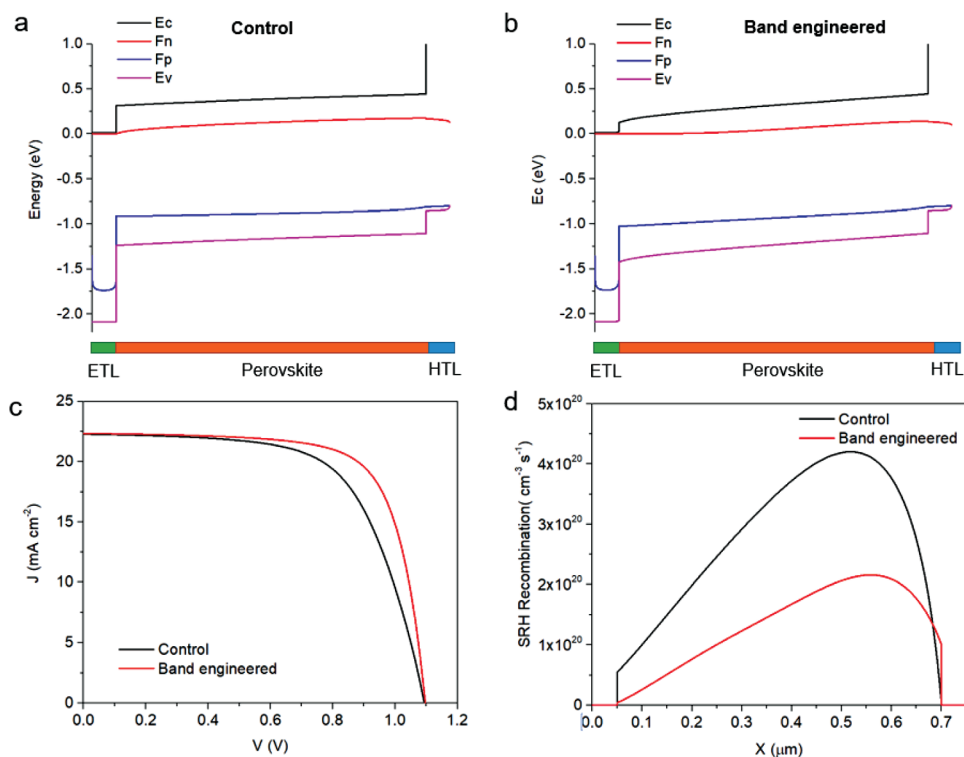


Figure 3. SCAPS-1D simulation results for band engineered and control devices. a,b) CBMs, VBMs, and electron and hole quasi-Fermi levels (Fn and Fp) for control (a) and band engineered devices (b), operating at a bias of 0.8 V, which is near MPP for real CsFA devices. c) Simulated J - V curves. d) Shockley-Read-Hall recombination rate across the perovskite region of the control and band engineered devices. Detailed parameters used in simulations are given in Table S2, Supporting Information.

has been used in previous reports to dope PCBM, improving conductivity.^[14,15] Here we find it can instead be used to achieve n-type doping of the perovskite itself, since the highest occupied molecular orbital of *N*-DPBI is higher in energy than the CBM of the perovskite, which should in principle enable electron transfer from *N*-DPBI to the perovskite (Figure 4a). The addition of *N*-DPBI into perovskite using the antisolvent can reasonably be expected to introduce a corresponding doping gradient within the film, with a higher concentration of dopant closer to the film surface. This should achieve the energetically-downward band bending of the perovskite CBM, creating an additional internal electric field within perovskite layer (Figure 4b), thus facilitates electron transfer.

To challenge this assumption, we proceeded to check the distribution of the *N*-DPBI dopant and to investigate its possible effect on charge transfer. We performed time-of-flight secondary ion mass spectrometry (TOF-SIMS) for the distribution (Figure S2, Supporting Information). The sample for TOF-SIMS was doped perovskite on indium tin oxide (ITO) substrate, and perovskite layer was sputtered between 0 and 1100 s until the rise of the In signal was observed. Figure S2a, Supporting Information reports sputtering spectra and Figure S2b, Supporting Information the zoomed in portion between 0 and 200 s. The DPBI ($C_{27}H_{25}N_3$) and its major fractions ($C_{27}H_{24}N_3$, C_6H_6 , and C_6H_5) give a fast-decreasing signal during 0–120 s; after 120 s of sputtering, these signals become very low. The gradient doping is thus in the top ≈ 70 nm of the perovskite film; there is little *N*-DPBI deeper into the sample. To ascertain

the doping type we used ultraviolet photoelectron spectroscopy (UPS) and compared the work function of undoped and doped perovskite film (Figure S3, Supporting Information). The work function of undoped perovskite is 4.5 eV, while that of *N*-DPBI doped perovskite is 4.0 eV. The lowered work function indicates a trend in the direction of n-type doping using *N*-DPBI.

We then performed PL quenching studies of doped perovskite/PCBM structures (Figure S4, Supporting Information). The quenching time τ_q obtained from fitting is 40 ns, 2.5 times faster than the $\tau_q = 106$ ns of undoped CsFA perovskite (Figure 2). The decreased quenching time illustrates faster charge transfer in the case of *N*-DPBI doped perovskite.

We fabricated PSCs with an architecture consisting of ITO/ NiO_x /CsFA/ C_{60} /Ag, where band engineered devices had CsFA active layers treated with *N*-DPBI (see Experimental Section). J - V curves for control and band-engineered PSCs are given in Figure 4b and Figure S5, Supporting Information. Compared to control devices, band engineered devices have improved FF (from 0.75 to 0.81), in agreement with simulation. The short-circuit current (J_{SC}) and open-circuit voltage (V_{OC}) are also improved (external quantum efficiency (EQE) data are given in Figure S6, Supporting Information). When operated at MPP, band-engineered devices exhibit a stabilized output of 20.3% (Figure 4c), a high efficiency for CsFA PSCs, while control devices have a PCE of 18% (Figure S7, Supporting Information). Impedance spectroscopy was performed to ascertain the impact of gradient doping (Figure S8, Supporting Information). The charge transfer time constant in the high frequency region

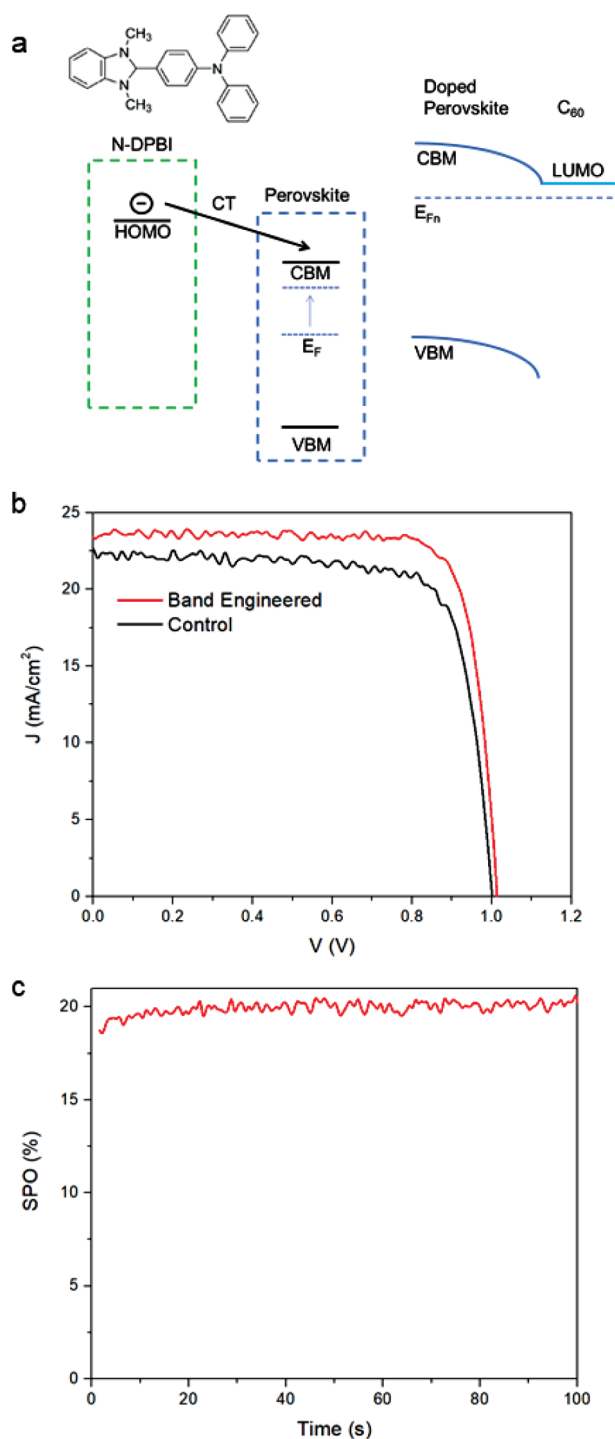


Figure 4. a) *N*-DPBI as perovskite molecular dopant. b) *J*–*V* curves of control and band engineered PSCs. c) SPO of the champion band engineered PSC.

is $t = R_{\tau}C_{\tau}$. For the band engineered device, $t = 6 \mu\text{s}$, smaller than the $t = 732 \mu\text{s}$ in the control device. This improved charge transfer seen in impedance spectra supports the picture of band engineered device design.

Compared to previously reported CsFA devices using *n*–*i*–*p* architectures and Spiro-OMeTAD as an hole transporting

layer (HTL),^[10,16,17] the architecture herein only contains materials stable at 85 °C.^[6,11] We investigated the stability of the band engineered CsFA PSCs. No significant degradation in PCE was observed following 275 h of MPP tracking at room temperature (Figure S9, Supporting Information). Unencapsulated devices retain 89% of their initial efficiency when heated at 85 °C (Figure S10, Supporting Information). The stability is attributed to the *p*–*i*–*n* structure that employs stable NiO_x and C₆₀/SnO₂ as transport layers.

3. Conclusions

The band-engineering strategy seeks to compensate for limited carrier transport in CsFA perovskites. Simulated and experimental device data both show increased performance attributable primarily to improved FF, consistent with enhanced extraction comparatively near to what are normally flat-band conditions. Simulations demonstrate that the design of the internal electric field facilitates charge transfer at MPP, reducing SRH recombination in active layers that otherwise suffer from poor carrier transport. The CsFA-based PSCs achieve a high SPO of 20.3% and can survive 85 °C heating test.

4. Experimental Section

Materials: CsI powder (99.999%), *N*-DPBI (98%) and anhydrous DMF, DMSO, and anisole were purchased from Sigma Aldrich. PbI₂ beads (99.999%), PbBr₂ powder (99.999%) were purchased from Alfa Aesar. FAI and MAI were purchased from GreatCell Solar. All salts and solvents were used as received without further purification.

Preparation of Perovskite Solution: For the CsMAFA perovskite CsI, MAI, FAI, PbI₂, and PbBr₂ were dissolved in a DMSO/DMF (1:4) mixture solution in the following molar ratios: PbI₂/PbBr₂ = 0.9:0.1, CsI/FAI/MAI = 0.05:0.81:0.14, and (FAI + MAI + CsI)/(PbI₂ + PbBr₂) = 1:1 to get the final concentration of 1.4 m. For CsFA perovskite, PbI₂/PbBr₂ = 0.9:0.1, CsI/FAI = 0.1:0.9, and (CsI + FAI)/(PbI₂ + PbBr₂) = 1:1, the final concentration was 1.4 m.

Perovskite Solar Cell Fabrication: Pre-patterned ITO (TFD Devices) coated glass was cleaned by sequential sonication in acetone and isopropanol. NiO_x thin film was deposited as HTL using method described by Hao et al.^[18] The perovskite film was spin-coated on NiO_x layer with a two-step procedure. The first step was 1000 rpm for 10 s with an acceleration of 200 rpm s⁻¹, and the second step was 6000 rpm for 30 s with a ramp-up of 2000 rpm s⁻¹. Anisole (100 μL) was dropped onto the spinning substrate during the second spin-coating step in the last 10 s of the second spin coating step. The substrates were then immediately transferred onto a hotplate and annealed at 100 °C for 30 min. For the band engineered device, *N*-DPBI was added into anisole with a concentration of 0.3 mg mL⁻¹, this will enable that *N*-DPBI enters the perovskite in the spin-coating process. 30 nm of evaporated C₆₀ and 25 nm of ALD deposited SnO₂ was used as ETL and finally 100 nm Ag was deposited as back contact.

Characterization: The *J*–*V* characteristics were measured using a Keithley 2400 sourcemeter under the illumination with a solar simulator (Newport, class A) at an intensity 100 mW cm⁻² in N₂ atmosphere (Sciencetech class A). Unless otherwise stated, the *J*–*V* curves were measured with a scanning rate of 100 mV s⁻¹ (voltage step of 10 mV and delay time of 100 ms). An aperture shade mask with an area of 4.9 mm² was placed in front of the solar cell device to avoid overestimation of the photocurrent density. The steady-state PCE, PCE(*t*), was measured by setting the bias voltage to the value at MPP (*V*_{MPP}) and then periodically measuring the current density. *V*_{MPP} was determined from the forward and reverse scanned *J*–*V* curves. A spectral mismatch factor of 1 was

used for all J - V measurements. EQE measurements were performed using Newport QUANTX-300 with monochromatic light and white bias light (≈ 0.1 Sun). The photodiode used for the calibration of EQE measurements has been calibrated by Newport. Stability and aging tests at continuous MPP operation under 1 Sun, AM 1.5 G illumination were carried out in nitrogen by fixing the voltage at V_{MPP} and then tracking the current output.

XRD patterns were obtained using a Rigaku MiniFlex 600 diffractometer equipped with an NaI scintillation counter and using monochromatized Copper $K\alpha$ radiation ($\lambda = 1.5406 \text{ \AA}$). PL lifetimes were measured using a Horiba Fluorolog time correlated single-photon-counting system with photomultiplier tube detectors. The excitation source was a laser diode at a wavelength of 504 nm. Perovskite film for PL lifetime measurement use a concentration of 1 M instead of 1.4 M for better signal, and the thickness was estimated to be $300 \pm 30 \text{ nm}$. TOF-SIMS was performed using ToF-SIMS5 from ION-TOF GmbH. (Munster, Germany). Samples were analyzed in dual beam profiling mode. All profiles were performed in non-interlaced mode. Spectral data were acquired in a high mass-resolution mode. The primary ion for analysis was 30 keV Bi_3^+ at 0.3 pA (Bi liquid metal ion source). This ion beam was applied over a $100 \mu\text{m} \times 100 \mu\text{m}$ area at the center of the sputter crater. The sputter ion was 1 keV Ar^+ at 120 nA (Ar, electron impact ion source). A $400 \mu\text{m} \times 400 \mu\text{m}$ sputter crater was used. The UPS measurement was conducted on a PHI 5500 Multi-technique system using a non-monochromated He $I\alpha$ photon source ($h\nu = 21.22 \text{ eV}$). The base pressure of the system was 10^{-9} torr. All the UPS measurements were carried out with a take-off angle of 88° and under a bias of -5 V . The impedance spectrum was measured using a potentiostat electrochemical workstation (AUT50690, PGSTAT204, the Netherlands) at different biases. The frequency ranged from 1 MHz to 1 Hz with 100 data points.

SCAPS Simulations: It was assumed the N -DPBI decays exponentially in its concentration going deeper into the bulk perovskite film. Since the free carrier density n in n -type doped semiconductor was mostly determined by the concentration of donors N_{d} , and n is proportional to $\exp(-(E_{\text{c}} - E_{\text{f}})/kT)$, the band structure of the doped perovskite could be regarded as linearly tilted at flat band. The detailed parameters are given in Table S2, Supporting Information.

Supporting Information

Supporting Information is available from the Wiley Online Library or from the author.

Acknowledgements

This work was supported by Ontario Research Fund-Research Excellence program (ORF7-Ministry of Research and Innovation, Ontario Research Fund-Research Excellence Round 7) and US Department of the Navy, Office of Naval Research (grant award no. N00014-17-1-2524).

Conflict of Interest

The authors declare no conflict of interest.

Keywords

carrier transport, CsFA, doping, perovskites, solar cells

Received: December 8, 2020

Published online:

- [1] NREL Efficiency Chart. <https://www.nrel.gov/pv/insights/assets/pdfs/cell-pv-eff-emergingpv.20200406.pdf> (accessed: January 2020)
- [2] E. H. Jung, N. J. Jeon, E. Y. Park, C. S. Moon, T. J. Shin, T.-Y. Yang, J. H. Noh, J. Seo, *Nature* **2019**, *567*, 511.
- [3] Q. Jiang, Y. Zhao, X. Zhang, X. Yang, Y. Chen, Z. Chu, Q. Ye, X. Li, Z. Yin, J. You, *Nat. Photonics* **2019**, *13*, 460.
- [4] X. Zheng, Y. Hou, C. Bao, J. Yin, F. Yuan, Z. Huang, K. Song, J. Liu, J. Troughton, N. Gasparini, C. Zhou, Y. Lin, D.-J. Xue, B. Chen, A. K. Johnston, N. Wei, M. N. Hedhili, M. Wei, A. Y. Alsalloum, P. Maity, B. Turedi, C. Yang, D. Baran, T. D. Anthopoulos, Y. Han, Z.-H. Lu, O. F. Mohammed, F. Gao, E. H. Sargent, O. M. Bakr, *Nat. Energy* **2020**, *5*, 131.
- [5] IEC 61215-1:2016 Terrestrial Photovoltaic (PV) Modules - Design Qualification and Type Approval - Part 1: Test Requirements, IEC Webstore, **2016**.
- [6] R. Cheacharoen, C. C. Boyd, G. F. Burkhard, T. Leijtens, J. A. Raiford, K. A. Bush, S. F. Bent, M. D. McGehee, *Sustainable Energy Fuels* **2018**, *2*, 2398.
- [7] B. Conings, J. Drijkoningen, N. Gauquelin, A. Babayigit, J. D'Haen, L. D'Olieslaeger, A. Ethirajan, J. Verbeeck, J. Manca, E. Mosconi, F. De Angelis, H.-G. Boyen, *Adv. Energy Mater.* **2015**, *5*, 1500477.
- [8] E. J. Juarez-Perez, Z. Hawash, S. R. Raga, L. K. Ono, Y. B. Qi, *Energy Environ. Sci.* **2016**, *9*, 3406.
- [9] K. A. Bush, A. F. Palmstrom, Z. J. Yu, M. Boccard, R. Cheacharoen, J. P. Mailoa, D. P. McMeekin, R. L. Z. Hoye, C. D. Bailie, T. Leijtens, I. M. Peters, M. C. Minichetti, N. Rolston, R. Prasanna, S. Sofia, D. Harwood, W. Ma, F. Moghadam, H. J. Snaith, T. Buonassisi, Z. C. Holman, S. F. Bent, M. D. McGehee, *Nat. Energy* **2017**, *2*, 17009.
- [10] S.-H. Turren-Cruz, A. Hagfeldt, M. Saliba, *Science* **2018**, *362*, 449.
- [11] R. Cheacharoen, N. Rolston, D. Harwood, K. A. Bush, R. H. Dauskardt, M. D. McGehee, *Energy Environ. Sci.* **2018**, *11*, 144.
- [12] M. I. Saidaminov, K. Williams, M. Wei, A. Johnston, R. Quintero-Bermudez, M. Vafaie, J. M. Pina, A. H. Proppe, Y. Hou, G. Walters, S. O. Kelley, W. A. Tisdale, E. H. Sargent, *Nat. Mater.* **2020**, *19*, 412.
- [13] E. M. Y. Lee, W. A. Tisdale, *J. Phys. Chem. C* **2015**, *119*, 9005.
- [14] Z. Wang, D. P. McMeekin, N. Sakai, S. van Reenen, K. Wojciechowski, J. B. Patel, M. B. Johnston, H. J. Snaith, *Adv. Mater.* **2017**, *29*, 1604186.
- [15] S. S. Kim, S. Bae, W. H. Jo, *Chem. Commun.* **2015**, *51*, 17413.
- [16] D. Yang, R. Yang, K. Wang, C. Wu, X. Zhu, J. Feng, X. Ren, G. Fang, S. Priya, S. Liu, *Nat. Commun.* **2018**, *9*, 3239.
- [17] H. W. Qiao, S. Yang, Y. Wang, X. Chen, T. Y. Wen, L. J. Tang, Q. Cheng, Y. Hou, H. Zhao, H. G. Yang, *Adv. Mater.* **2019**, *31*, 1804217.
- [18] H. Chen, Q. Wei, M. I. Saidaminov, F. Wang, A. Johnston, Y. Hou, Z. Peng, K. Xu, W. Zhou, Z. Liu, L. Qiao, X. Wang, S. Xu, J. Li, R. Long, Y. Ke, E. H. Sargent, Z. Ning, *Adv. Mater.* **2019**, *31*, 1903559.